



Materials and Energy Research Center
MERC

Contents lists available at [ACERP](#)

Advanced Ceramics Progress

Journal Homepage: www.acerp.ir



Original Research Article

Nanoindentation-Based Mechanical Properties Evaluation of Nano-Structure and Composite Plasma Spray Formed Ceramic Nozzles

Sana Seifollahpour ^a, Afshin Ashofteh ^{b,*}, Amir Hossein Shahdadi ^c, Mahmoud Mosavi Mashhadi ^d

^a MSc, School of Mechanical Engineering, College of Engineering, University of Tehran, Tehran, Tehran, Iran

^b Assistant Professor, Mahallat Institute of Higher Education, Mahallat, Markazi, Iran

^c PhD, School of Mechanical Engineering, Sharif University of Technology, Tehran, Tehran, Iran

^d Professor, School of Mechanical Engineering, College of Engineering, University of Tehran, Tehran, Tehran, Iran

* Corresponding Author Email: a.ashofteh@mahallat.ac.ir (A. Ashofteh)

URL: https://www.acerp.ir/article_170954.html

ARTICLE INFO

ABSTRACT

Article History:

Received 28 February 2023
Received in revised form 28 April 2023
Accepted 07 May 2023

Keywords:

Nano Indentation
Plasma Spray Forming
Ceramics
Composites

Ceramic nozzles are unique options in aerospace industry due to their ability to operate at high temperatures. However, their brittleness, structural defects, poor formability, and need for complex methods for measuring their mechanical properties are among the main obstacles to their development. In this study, four different conical nozzles were produced through Plasma Spray Forming (PSF). Given that Yttria-Stabilized Zirconia (YSZ) is one of the most common materials in high-temperature applications, it is considered as the base material. Throughout the research, three YSZ alternatives were investigated by changing the chemical composition (Ceria-Yttria co-Stabilized Zirconia (CYSZ)), by changing the particle size (nanostructured YSZ), and by double layer architecture design. The mechanical properties of the conical nozzles were then evaluated by the nanoindentation test using Oliver and Pharr method. This method can be quick and applicable for evaluation of the mechanical properties of ceramic parts based on the load-depth curve. X-Ray Diffraction (XRD) and Scanning Electron Microscopy (SEM) were performed for the phase analysis and coating microstructure and porosities investigation. The results highlighted the promising features of nano-structured YSZ that are strongly based on the presence of nano-zones inside the coating structure.



<https://doi.org/10.30501/acp.2023.387714.1121>

1. INTRODUCTION

Plasma spraying is a popular deposition method for materials with very high melting point such as ceramics that has been widely used in different industries due to its inexpensiveness (relatively low cost), high velocity, and suitable quality. The deposition process involves melting a ceramic powder using a high-temperature plasma stream, shooting the molten particles to the substrate, and

forming a dense layer. The plasma jet consists of three hot, moderate, and cold regions, depending on the location. A particle can hit the substrate in a melted, semi-melted, and unmelted forms. The most common case of this method application is creation of barrier coatings against oxidation, corrosion, high temperature, etc. [1]. The porous films created by this method are widely used in the automotive, aerospace, and power generation industries, and there are increasing demands

Please cite this article as: Seifollahpour, S., Ashofteh, A., Shahdadi, A., Mosavi Mashhadi, M., "Nanoindentation-Based Mechanical Properties Evaluation of Nano-Structure and Composite Plasma Spray Formed Ceramic Nozzles", *Advanced Ceramics Progress*, Vol. 9, No. 2, (2023), 24-35. <https://doi.org/10.30501/acp.2023.387714.1121>

2423-7485/© 2023 The Author(s). Published by MERC.

This is an open access article under the CC BY license (<https://creativecommons.org/licenses/by/4.0/>).



for their improvements to reach advanced functionality and durability [2]. Therefore, plasma-sprayed coatings protect the substrate from damages in working conditions. On the contrary, the substrate supports the brittle coating. However, this combination can be the source of some damages caused by the inconsistency of the physical and mechanical properties of the substrate (mainly metallic) and the coating (mainly ceramic) [3]. For example, in thermal cycles, Coefficient of Thermal Expansion (CTE) mismatch between the two layers can cause cracks in the coating. In working conditions with limited mechanical loads, the coating can withstand without the substrate support and consequently, separation of the coating from the substrate can prevent any thermal and functional mismatch. An example of Plasma Spray Forming (PSF) is production of high-temperature ceramic nozzles [4].

Nanoindentation technique is an effective procedure for measuring the mechanical properties of materials even in its small volumes and wide acceptance arising from the improvements made within this technique [5]. Nanoindentation is an applicable method for investigating nano-scale mechanical properties such as hardness or Young's modulus and also dislocation nucleation at the nanoscale [6]. Nanoindentation forces the indenter tip into the surface and measures the reflected response and created mark. Mechanical characterization of the phases has an evident advantage [7], and Nanoindentation is an ideal method for measuring material properties at sub-micrometer scales by applying small loads, thus enabling the individual identification of each phase in heterogeneous cases. [8-10]. It can also be very effective for thin films and micro-/nano-electromechanical system (MEMS/NEMS) devices [11,12] that, along with other methods, measures the complex compliance of linearly viscoelastic materials [13,14]. Indenter geometry and variation in a testing method have been already discussed in some works [15,16]. Based on these studies, it can be concluded that this method can be practically and effectively used in ceramic coatings like YSZ fabricated by different methods such as EB-PVD or APS [17-20]. Nanoindentation is also practical in measuring through-thickness and in-plane properties of multi- and single-layer nanocomposite films [21-23]. A literature survey revealed many reports that compared the deposited and bulk properties of ceramics with those of nanoindentation [24]. The potentials of this method are the properties and structural features evaluation of the composites and nanocomposites [25-31].

Owing to its relatively high CTE and low thermal conductivity, YSZ is usually used as a thermal protector at temperatures above 1100 °C. In addition, Ceria-Yttria co-Stabilized Zirconia (CYSZ) is commonly used as a thermal barrier coating on the hot parts of a combustion chamber and the first row of the turbine blades owing to its resistance to thermal shock, low thermal conductivity,

good wear resistance, and high resistance to hot corrosion. According to some research studies, Ceria-Stabilized Zirconia (CSZ) is characterized by more toughness and better thermal shock resistance than YSZ. In addition, yttria is more costly than ceria. The main weakness of CSZ is its significantly lower erosion resistance. Mixing Ceria with Yttria as co-stabilizers and creating CYSZ is a solution that combines the properties of both materials and offers advanced performance [1].

Nanostructured coatings exhibit improved performance due to nano zones. Compared to the conventional coatings, the overall porosity in these coatings does not change much but their distribution becomes uniform in terms of size and position. In material engineering and design, composite and nano-structure coatings are solutions that are considered in many cases [32,33].

In this study, the properties of the YSZ ceramic nozzles are considered as the base, and the effect of changes in the chemical composition, nano structuration, and architecture on the mechanical properties were investigated. In this regard, CYSZ, nanostructured YSZ (YSZ-N), and a layered composite of YSZ-N and CYSZ were first produced by PSF and then, their hardness and elastic modulus were calculated using Oliver-Pharr technique. Based on the results of Nanoindentation, X-Ray Diffraction (XRD), and Scanning Electron Microscopy (SEM) images, the performance and the reasons behind such mechanisms were elaborated.

2. MATERIALS AND METHODS

2.1. Materials

In this study, three different powders including nano- and micro-structured YSZ and CYSZ (Table 1) were used, and the effect of changing different factors on the performance of YSZ, the current conventional material in many high-temperature applications, was investigated.

- Changing the chemical composition by using CYSZ
- Changing microstructure by YSZ nano-structuring (YSZ-N)

Changing the architecture by producing a layered composite structure consisting of YSZ-N and CYSZ.

Accordingly, four different conical ceramic nozzles of YSZ, YSZ-N, and CYSZ, and a composite of YSZ-N and CYSZ were produced by plasma spray forming.

2.2. Mandrel Design

The mandrel was a hollow tapered cylinder with a small slope along its length made from Al 6061 (Figure 1).

The tapered design of the mandrel facilitates the separation process. Aluminum 6061 has a CTE of about $25 \times 10^{-6} \text{ }^\circ\text{C}$ which is approximately 2.5 times higher than that of YSZ (10×10^{-6} [34]) and CYSZ. If the mandrel has proper roughness (in our case $0.67 \pm 0.1 \text{ } \mu\text{m}$), different CTEs of the deposited layer and substrate

facilitate better separation. More surface roughness can cause strong mechanical bonds and cracks during cooling

while quite low roughness will decrease the deposition efficiency.

TABLE 1. Characteristics of ceramic powders

	YSZ	CYSZ	YSZ-NANO
Full Name	Yttria Stabilized Zirconia	Ceria-yttria co-stabilized zirconia	Yttria Stabilized Zirconia-nano structured
Formula	ZrO ₂ -8 wt. % Y ₂ O ₃	ZrO ₂ 24CeO ₂ 2.5Y ₂ O ₃	ZrO ₂ -8 wt. % Y ₂ O ₃
Producer	METCO 234A	METCO 205NS	INFRAMAT Nanox TM S4007
Shape	spherical	spherical	spherical
Density	1.8 – 2.4 g/cm ³	2.2 ± 0.1 g/cm ³	1.4 - 1.7 g/cm ³
Melting point	about 2800 °C	about 2800 °C	about 2800 °C
Particle size	50-70 μm	40-50 μm	< 100 nm (agglomerated size: 15-150 μm)

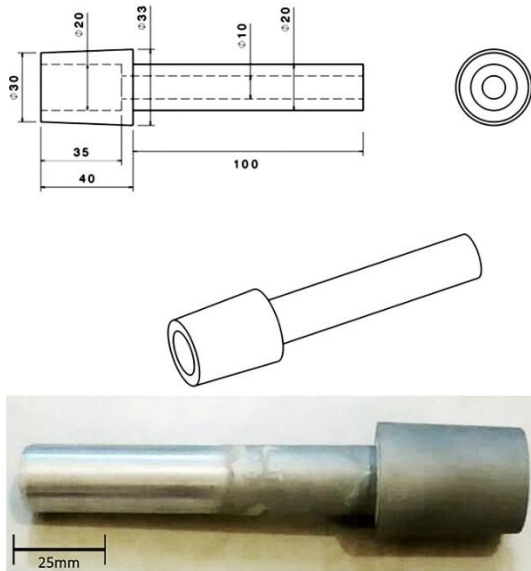


Figure 1. Mandrel used in the plasma spray forming process

2.3. Plasma Spraying

At the beginning of the deposition process, the mandrel was sandblasted with alumina to increase the adhesion of the molten powders to the surface. In the next step, the mandrel was preheated at 200 °C without feeding the powder to prevent thermal shock and damage. In the main spraying process, powders enter the plasma where they melt and accelerate at a very high speed. These melted particles sit on the rotating mandrel and with the linear movement of the spraying gun, a layer will be formed. At the end of each linear movement of the gun, it pauses for 15 seconds to release the residual stresses and then, the next cycle begins. This time allows the stress to release by providing the needed time for heat transfer. Of note, longer pause causes loose connections. The thickness of each deposition round is approximately 100-150 μm. To reach the desired thickness (in this study 450 μm), the deposition process was run three times. Once the process is complete, the coated mandrel is post-heated at 200 °C without powder to prevent cracking and then, it opens from the APS machine and cools down quickly. Plasma spraying parameters were selected in

consultation with experts based on conventional values in high-temperature applications. More details are given in Table 2.

Table 2. Plasma spraying parameters

Parameter	YSZ	CYSZ	YSZ-N
Current (A)	600	600	600
Voltage (V)	55	55	55
Primary gas flow (Ar) (nlpm*)	40	42	35
Secondary gas flow (H ₂) (nlpm)	9	9	9
Carrier gas flow (Ar) (nlpm)	2.5	2.5	2.5
Powder feed rate (gr/min)	50	40	50
Spray distance (mm)	150	150	100
Rotation speed (RPM)	120	120	120
Surface roughness (μm)	0.67±0.1	0.67±0.1	0.67±0.1

* Normal Liter Per Minute

2.4. Separation

The important part of the process is the coating separation from the mandrel. For this purpose, the mandrel is immersed in liquid nitrogen. The difference in the CTE of both mandrel and coating, as well as the conical shape, causes the coating separation. The higher surface roughness, as previously assumed to be essential for successful deposition, can be a reason for the complexity of the separation process. According to Figure 2-b, the ceramic coating is easily separated from the conical part of the mandrel but the part of the coating that was formed on the cylindrical trail of the mandrel is not separated from it. This is another confirmation of the importance of the conical geometry of the mandrel.

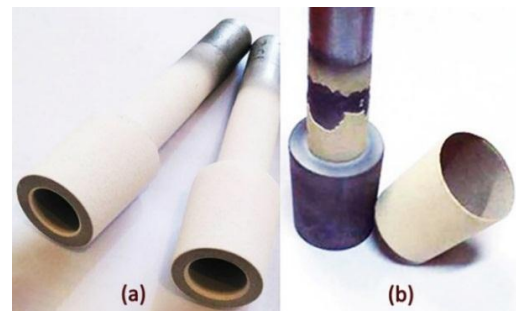


Figure 2. (a) Coated mandrel and (b) nozzle separated from the mandrel

2.5 Theoretical Background

The nanoindentation test involves an indenter (in this study, pyramid-shaped with angle $\alpha = 136^\circ$) that penetrates into the surface to a specified load or depth. Then, it is unloaded as a result of which, penetration depth (h) is measured as a function of load (P). Figure 3 shows an example of the notch created in this test on the polished section of coating.

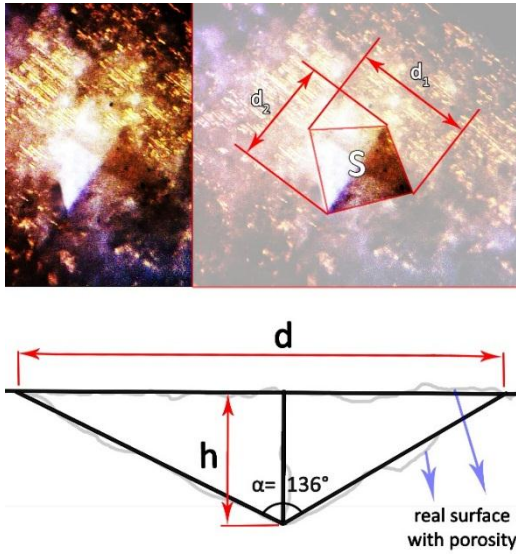


Figure 3. The indenter effect on the surface along with the schematic representation of important elements

Given that the microstructure of the plasma-sprayed ceramic materials is porous, d_1 and d_2 are slightly different from each other. For ease of calculation, their average value $((d_1+d_2)/2)$ is considered as d . Consequently, h can be calculated by Equation (1):

$$\tan\left(\frac{\alpha}{2}\right) = \frac{d}{h} = \frac{\left(\frac{d_1+d_2}{2}\right)}{h} \rightarrow h = \frac{\left(\frac{d_1+d_2}{4}\right)}{\tan\left(\frac{\alpha}{2}\right)} \cong \frac{\left(\frac{d_1+d_2}{4}\right)}{2.475} \quad (1)$$

$$\rightarrow h \cong \frac{d_1 + d_2}{9.9}$$

Equation (2) shows the projected area of the indented region (S):

$$S = \frac{d_1 \times d_2}{2} \approx \frac{d^2}{2} \approx \frac{(4.95 h)^2}{2} \approx 12.25 h^2 \quad (2)$$

Considering the load P and consequence projected area S , we can measure the hardness HV at that load from Equation (3) [35]:

$$HV = \frac{2 P \sin \frac{136^\circ}{2}}{d^2} = \frac{1.8544 P}{d^2} \quad [\text{kgf/mm}^2] \quad (3)$$

Figure 4 is a typical load-penetration depth curve in which the starting point of the loading process is the origin (O). Followed by applying the load, a diagram similar to L_1 is traversed. After reaching the maximum load (A), the load remains constant while h increases a little (L_2). Once the value of h becomes fixed, unloading begins (L_3). At the end of the path (point C , the load is zero), a residual amount of h will be formed which represents the plastic deformation of the sample. It corresponds to what happens in the stress-strain diagram after removing the load in the plastic area.

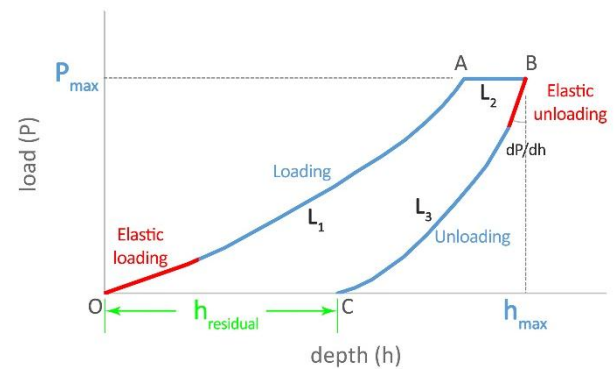


Figure 4. Nanoindentation load-depth curve

Three important parameters must be measured from the P - h curve:

- P_{max} : the maximum load
- h_{max} : the maximum penetration depth
- $\gamma = \frac{dP}{dh}$: the elastic unloading stiffness, defined as the slope of the elastic unloading curve

The quality and preciseness of measurement strongly depend on the experimental measurement of parameters [36]. In this test, the loading and unloading rates are similar but the slopes of the elastic loading and unloading are independent of each other that are determined considering the properties of the material.

The effective elastic modulus, E_f , is calculated using the γ and the S , as shown in Equation (4):

$$E_f = \frac{\sqrt{\pi} \gamma}{2 \beta \sqrt{S}} \quad (4)$$

In the above equation, β has a constant value according to the indenter. Traditionally, this parameter compensates for the stiffness deviations caused by the asymmetry of the pyramidal indenters. It should be noted that β is dimensionless and is normally taken as 1 [33], hence $\beta=1$ in the present study. Reduced modulus (E_r) shows that the measured displacement is a combination of both indenter and sample. Given that, the elastic modulus of the sample (E) can be calculated using the Poisson's ratio of the sample (ν), modulus of the indenter (E_i), and

Poisson's ratio of the indenter (ν_i). The effective elastic modulus is as shown in Equation. (5):

$$\frac{1}{E_f} = \frac{1 - \nu^2}{E} + \frac{1 - \nu_i^2}{E_i} \quad (5)$$

Diamond indenter has $E_i = 1140$ GPa and $\nu_i = 0.07$. The Poisson's ratio of the sample must come from tests on the bulk material or an estimation.

3. RESULTS AND DISCUSSION

In the layered composite structure, CYSZ provides toughness and shock resistance on the working surface, and YSZ works as a support. Given the lower price of CYSZ, it can be concluded that this change can also have cost-reduction effects. Figure 5 represents the SEM image of the elements contained in it. Porosity, which can be seen as the black areas in the image, is formed between the splats during spraying but the vertical cracks are mainly caused by shrinkage after the spraying process [37]. The amounts of Y are 5 % in the upper layer and 1.2 % in the lower layer, which decreased by 76 %. In addition, Zr decreased from 71.3 % to 57.5 %, which is a 19.4 % decrease. This difference is fully evident in Figure 6. In the analysis of the YSZ layer, the amount of Y is only 5 %; however, in the CYSZ layer, the sum of Ce and Y values is equal to 21.3 %.

To check the mechanical properties of the four produced nozzles, the cross-section of each sample was mounted. The indentation effect is smaller than the structural defects such as pores in the coating. In this study, nanoindentation tests were repeated five times, and the average of the obtained results was taken into account (Table 3).

Consideration of the number of repetitions is necessary because the ceramic samples produced by the plasma spraying method have inherently various structural defects and consequently, the properties and microscopic behavior of the material are slightly different at various points. The obtained results are listed in Table 3. In these samples, the largest diameter and depth of the notch were related to the nanostructured YSZ sample, and the

composite, CYSZ, and conventional YSZ samples are in the next ranks. These opposite results were obtained for hardness. According to the findings, the nano-structuration of YSZ would cause extensive changes in properties. A thorough examination of the microstructures shows that in the nano-structured samples, porosities are more uniformly distributed, some of which are present in the nano zones. In these coatings, 16.2 % of the area belongs to nano zones.

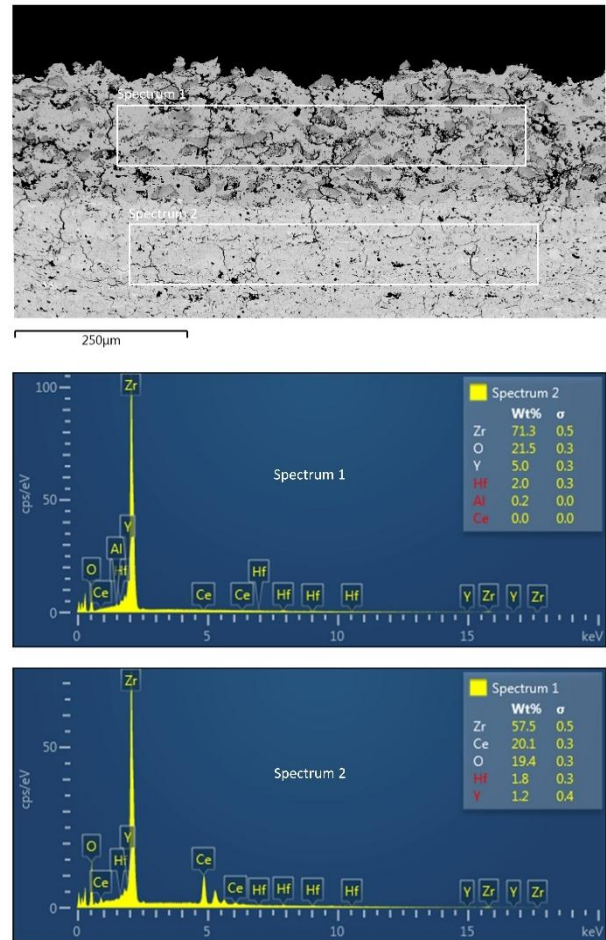


Figure 5. Percentage of elements in the exposed areas in the double-layer composite sample

Table 3. Hardness and depth of the notch for 100g load

	d* (at P=100 g) (μm)						HV (kgf/mm ²)						h** (μm)					
	T1***	T2	T3	T4	T5	Av.	T1	T2	T3	T4	T5	Av.	T1	T2	T3	T4	T5	Av.
YSZ	12.2	12.7	12.6	11.9	12.5	12.4	12.5	11.5	11.7	13.1	11.9	12.1	2.5	2.6	2.5	2.4	2.5	2.5
CYSZ	13.8	13.9	14.2	13.9	14.1	14	9.7	9.6	9.2	9.6	9.3	9.5	2.8	2.8	2.9	2.8	2.8	2.8
YSZ-N	20.2	21	12.7	19.8	12.7	17.3	4.5	4.2	11.5	4.7	11.5	6.2	4.1	4.2	2.6	4	2.6	3.5
C-YN	13.2	19.6	18.2	16.1	14.7	16.4	10.6	4.8	5.6	7.2	8.6	6.9	2.7	4	3.7	3.3	3	3.3

* Average diameter of the pyramid indenter

** Penetration depth

*** Test number 1

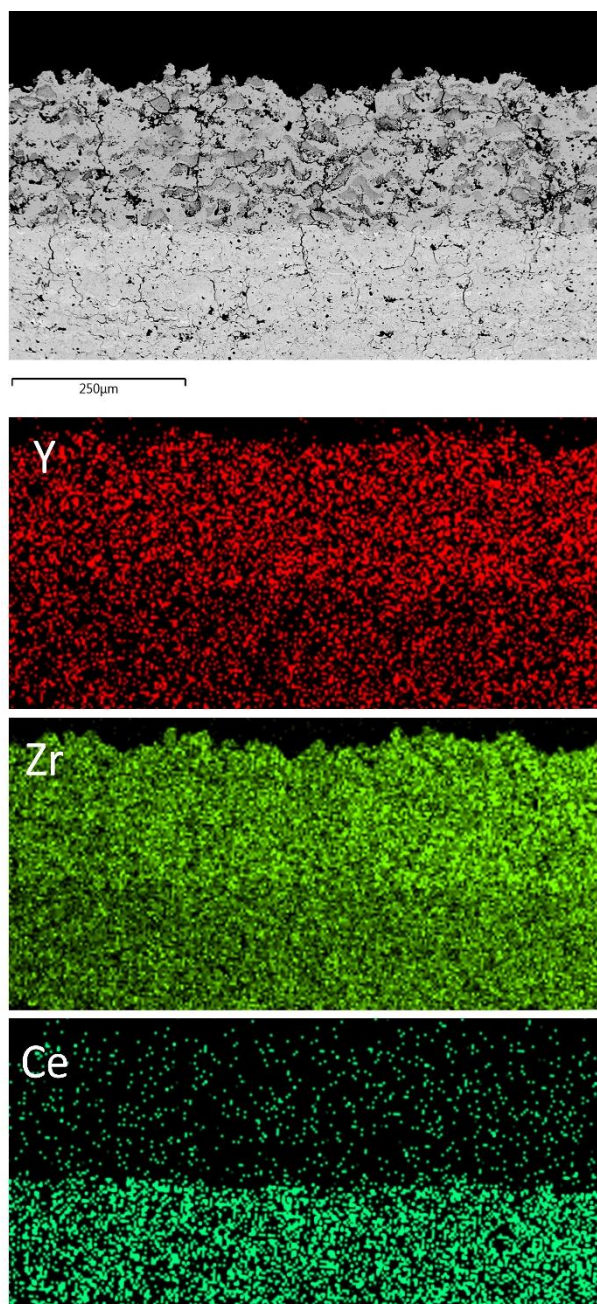


Figure 6. Distribution of elements in each layer of the double-layer composite sample

Nano zones consist of a large number of nanoparticles in nano dimensions that are uniformly distributed. Figure 7 shows the nano zones with high magnification and based on the particle size in this area, it can be concluded that particles will remain nano-structured during the deposition process.

This necessity exists in nanostructure and composite samples with greater intensity. Some samples were also mounted at about 45° angle to check whether there was a difference in the properties of the material in the planes that were angled compared to the perpendicular ones.

Further investigations show that the average results do not differ much in different planes but similar to the vertical plane, the results are slightly different in different locations.

The first investigation was carried out by applying a 100 g load on samples and checking the hardness and depth of the indentation.

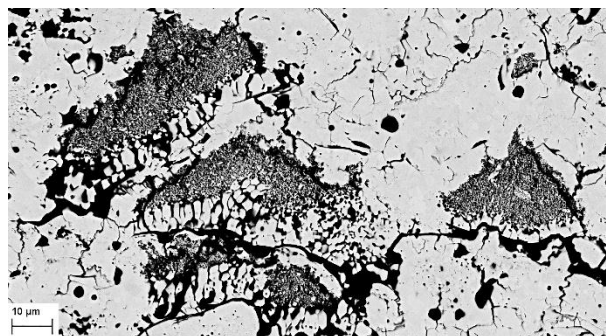


Figure 7. Nano zones with high magnification

As illustrated in the above pictures, large porosities are not observed in these areas (unlike the conventional type). In addition, these areas reduced the brittleness of the structure by creating a barrier against crack growth. As observed in Figure 8, many cracks in the structure stop or change their direction upon reaching the nano regions.

To create nano zones, the spraying parameters must be carefully adjusted at the time of layer deposition. As a result, a part of the nano-powders will be melted while the rest will remain unmelted. In the case of more melting, there is a narrow range where the nanostructure will be destroyed, and the coating will be micro-structured. On the contrary, in case few particles are melted, the connection and integrity of the coating will not be well formed. The adjusted parameters for the powders of this study are given in Table 2. The proper distribution of these particles on the coating surface causes final product gain more structural strength and less brittleness in addition to having the properties of conventional YSZ coatings.

The main elements in the microstructure of each sample are:

- YSZ: The porosities and cracks are distributed in the structure but porosities play the main role in its performance. Among all four samples in this study, the highest porosity is related to this material (Table 4).
- CYSZ: This coating has a denser structure containing porosities with smaller dimensions and better distribution; however, the number of these structural cracks are more than that of YSZ that play the main role in its performance.
- YSZ-N: The main factor causing differences in the performance of this material is the nano zones that in turn create a more uniform microstructure.

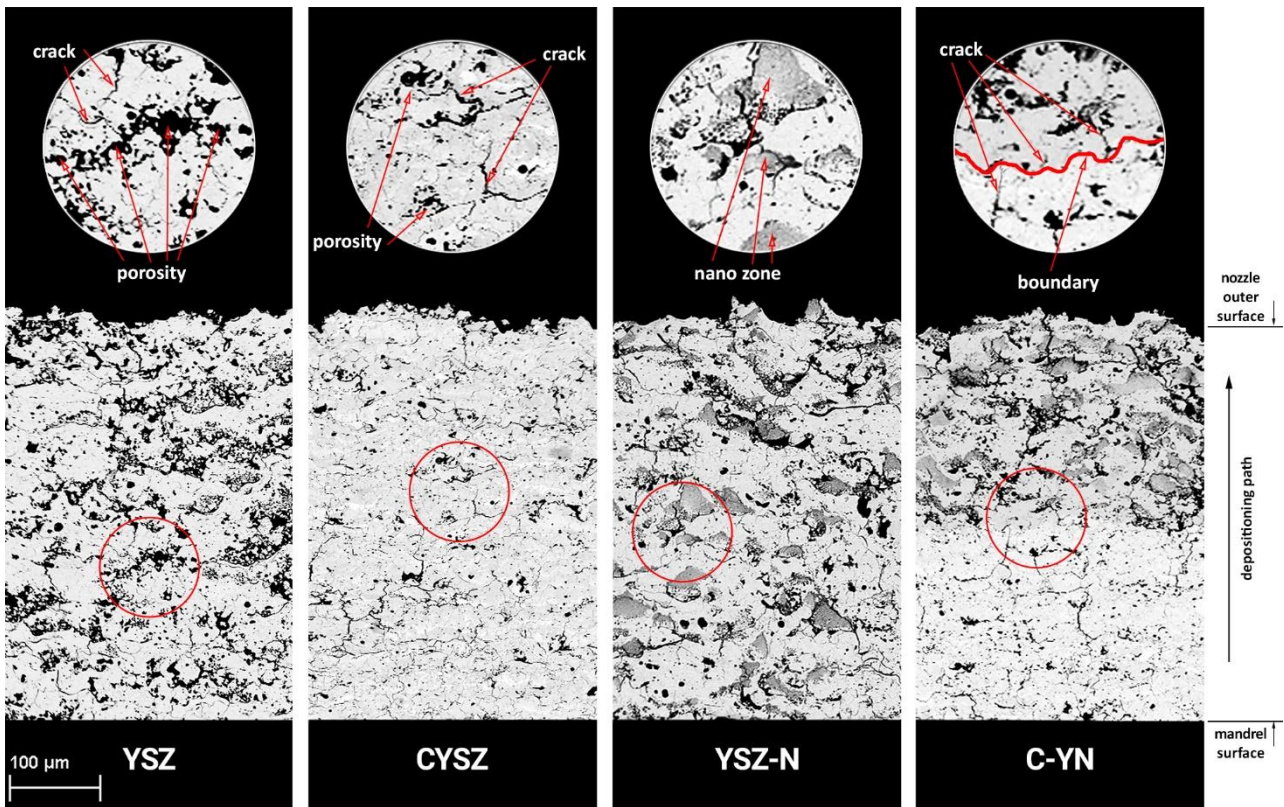


Figure 8. Cross-sectional SEM image of the four samples

- C-YN: The layer boundary plays the main role in this sample. The presence of this element controls the cracks and any damages. If a crack grows in a double-layer structure from the outer surface along the thickness, it will be stopped/weakened after reaching the layer boundary. Figure 8 demonstrates some cracks that stop after reaching the layer boundary.

In all samples, porosities are almost uniformly distributed (Figure 8) and according to Table 4, the amount of porosity has a direct relationship with the hardness. A comparison of the porosity of both YSZ and YSZ-N shows that they are of the same material that fully explains the importance of this parameter.

Table 4. Porosity and hardness of all samples [38,39]

	HV (kgf/mm ²)	Porosity (%)
YSZ	12.1	18.44
CYSZ	9.5	14.24
YSZ-N	6.2	9.61
C-YN	6.9	11.92*

*average value of YSZ-N and C-YN

Figure 9 shows the change of the effect of applying different loads on the sample surface. In case the indenter is placed inside the material, plastic and elastic deformations will happen and after exiting the indenter, the elastic deformation will be removed (Figure 10).

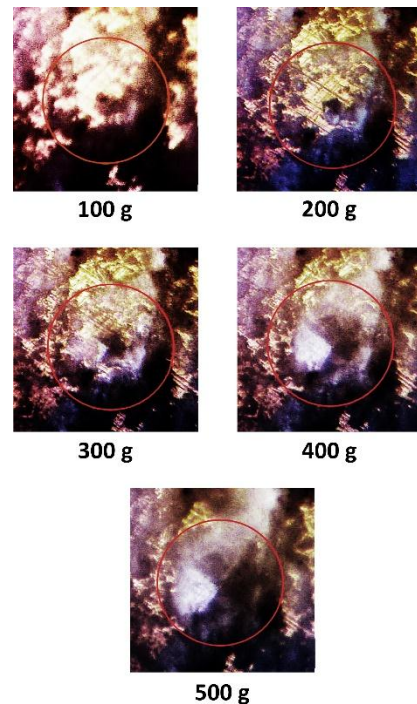


Figure 9. Changing the effect of the indenter by increasing the load

Due to the structural defects, the created notch is not

exactly symmetrical, and its dimensions are slightly different.

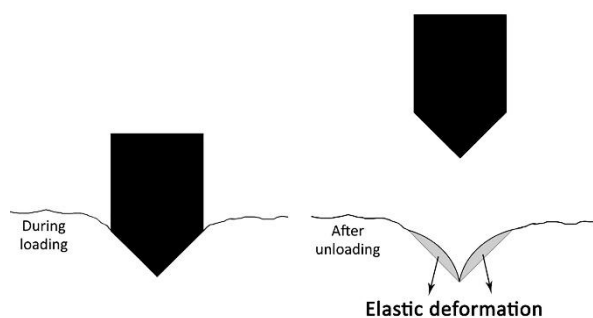


Figure 10. Schematic representation of elastic and plastic deformations during the nanoindentation process

In the ceramic samples, due to the brittleness and complexity of making the tensile test sample, it is practically difficult to measure the elastic modulus by the conventional methods; therefore, alternative methods such as the nanoindentation test are used. For this purpose, followed by applying a load and creating a notch in the material and then removing the load and checking the final notch, the elastic modulus can be determined. Table 5 presents the test results during loading and unloading. Figure 11 illustrates the graph of four tested samples. According to the obtained results and calculation of the elastic modulus based on the theoretical background relations, the reduced and elastic moduli of the samples are given in Table 6.

Table 5. Changing the depth of the notch during the loading and unloading stages

P (g)	YSZ		CYSZ			YSZ-N			C-YN		
	h (μm)		P	h (μm)		P	h (μm)		P	h (μm)	
	L*	UL**		L	UL		L	UL		L	UL
0	0	6.9	0	0	8.1	0	0	9.5	0	0	9.2
100	2.5	8.4	100	2.8	9.3	100	3.5	11.4	100	3.3	10.6
200	5.1	9.1	200	5.4	10	200	6.6	12.6	200	6.3	11.6
300	7.1	9.7	300	7.4	10.5	300	9.3	13.4	300	8.8	12.2
400	8.6	10.1	400	9.2	10.9	400	11.7	13.9	400	10.8	12.8
500	10.1	10.4	500	11	11.2	500	13.6	14.1	500	12.7	13.1
500	10.4		500	11.2		500	14.1		500	13.1	

*: Loading **:Unloading

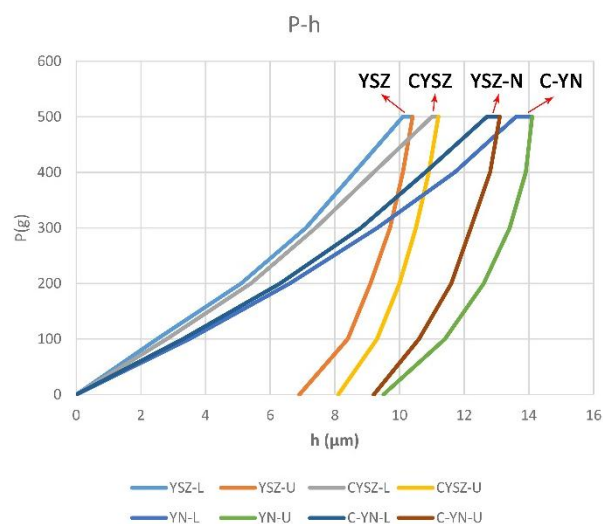


Figure 11. Loading and unloading curve

Table 6. Reduced elastic modulus (E_r) and elastic modulus (E)

	YSZ	CYSZ	YSZ-N	C-YN
E_r (GPa)	122.3	104.2	133.2	91.7
E (GPa)	130.3	107.4	143.5	94

On the one hand, there is a nanostructured layer with proper distribution and nano zones, which shows extraordinary characteristics. On the other hand, there is a CYSZ layer with a denser structure and more structural cracks. Despite the lowest L_2 length of CYSZ (a region where under a constant load, h advances slightly) in the graphs illustrated in Figure 11, the nanostructured and composite samples have the highest L_2 . In the nanostructure sample, the nano zones provide the context for more deformation in this area due to the structural order and integrity as well as lack of obstacles to deformation. In the composite sample, the presence of the layer boundary causes deformation because the layer boundary has less structural integrity, hence vulnerable to loads.

Based on the results, nano-structuring of YSZ enhances the elastic modulus up to about 10%. Of note, the double-layer structure has a much lower modulus due to its layered structure and difference in the properties of the two layers. The calculated results are comparable with other references that are mainly in the range of 50 GPa-250 GPa [40-45].

The XRD test results reveal that the monoclinic zirconia phase is presented in all samples before spraying.

After deposition, this phase disappears, and only a limited amount in YSZ will remain due to its transformation into a non-convertible tetragonal phase.

In YSZ, the wide peaks are attributed to the incorporation of some Zirconium Oxide (c) and Yttrium Zirconium Oxide (t) peaks near each other.

According to the Rietveld analysis, the most important phase of the YSZ is tetragonal Yttrium Zirconium Oxide (Figure. 12 and Table 7) formed as a result of the high cooling rate of the molten droplets during deposition. The wide peaks in 2θ about 35° , 60° , 75° , 82° , and 85° is the proof of the formation of tetragonal Yttrium Zirconium Oxide. In YSZ, tetragonal ZrO_2 peaks cannot be identified but cubic ZrO_2 peaks are detected, which the reason is why the number of the peaks of this material is higher than those of other samples.

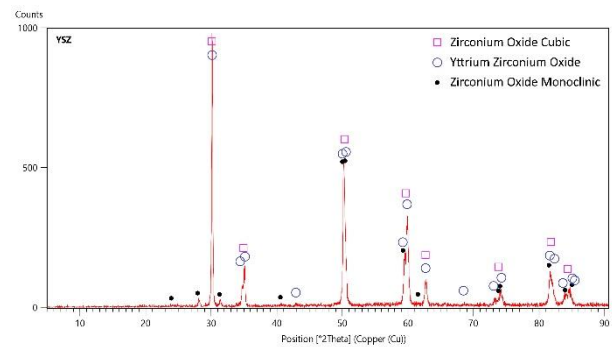


Figure 12. YSZ XRD test results

Table 7. Properties and percentage of phases in XRD results (based on the Rietveld analysis)

	Crystal System	Unit Cell Parameters				Materials		
		a*	c*	c/a	Volume**	YSZ	CYSZ	C-YN
Zirconium Oxide (c)	Cubic	5.175	5.175	1	138.581	30.8 %	16.5 %	21.8 %
Zirconium Oxide (t)	Tetragonal	3.641	5.218	1.433	69.189	-	81.5 %	27.8 %
Zirconium Oxide (m)	Monoclinic	5.210	5.370	1.03	145.16	0.7 %	-	-
Yttrium Zirconium Oxide	Tetragonal	3.613	5.162	1.429	67.482	68.5 %	0.4 %	47 %
Cerium	Cubic	5.161	5.161	1	137.468	-	1.6 %	3.4 %

*: 10^2 pm

** : 10^6 pm³

Both CYSZ and C-YN contain a small amount of Cerium with a cubic structure because the weight percentage of CeO_2 decreases due to its vaporization in the plasma area. In addition, the tetragonal phases in these samples do not have any shift because their unit cell volume is much smaller (about half) than that of other phases. In the presence of Ce, cubic ZrO_2 has a left phase shift in smaller 2θ and a right shift in greater 2θ resulting from the residual stress during deposition and rapid cooling. The main phase of the CYSZ is ZrO_2 (t) (Figure. 13), and its intensity is less than that of other phases with the highest number of peaks. YSZ sample contains only cubic zirconia but the samples containing CYSZ contain tetragonal ZrO_2 peaks due to the stability of the phases with CeO_2 . In CYSZ, a slight phase transition from monoclinic to tetragonal increases the thermal shock resistance. The main crystal system of all samples is tetragonal while the cubic ZrO_2 is still visible (Fig. 14).

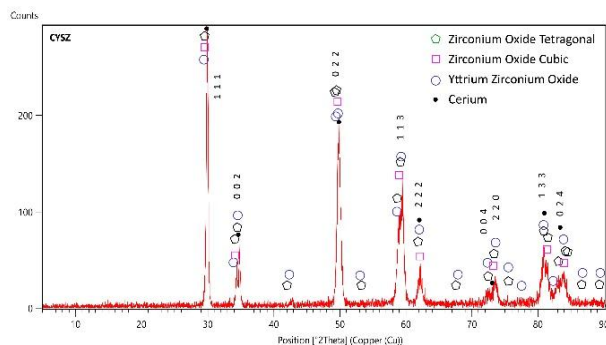


Figure 13. CYSZ XRD test results

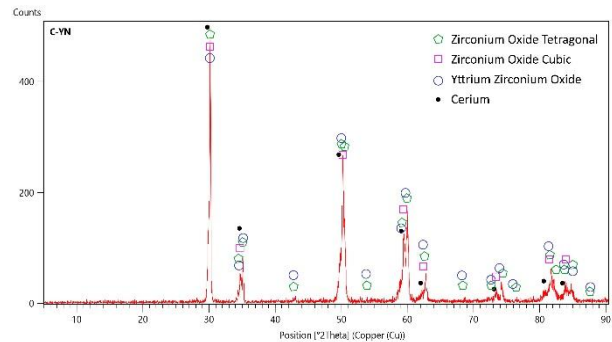


Figure 14. C-YN XRD test results

A comparison of the graphs shows that due to the higher volume fraction of the ZrO_2 (c) phase, the peaks in both YSZ and CYSZ are more intense than those of their counterparts. However, the presence of ZrO_2 (t) causes wider peaks in CYSZ and C-YN and in the CYSZ, where this phase is about 81.5 %, the phases are in a wider state with lower intensity and higher number of peaks.

The results from Raman analysis (Figure 15) confirm the formation of the tetragonal phase in the samples. In this figure, CYSZ, which has the highest degree of tetragonal phase, has the most intense peaks while on the opposite side, YSZ has the least intense peaks. In YSZ and at Raman shift 1000 (Cm^{-1}), a wide peak is observed, confirming the higher percentage of cubic structure in this material; however, this peak is very weak in other samples.

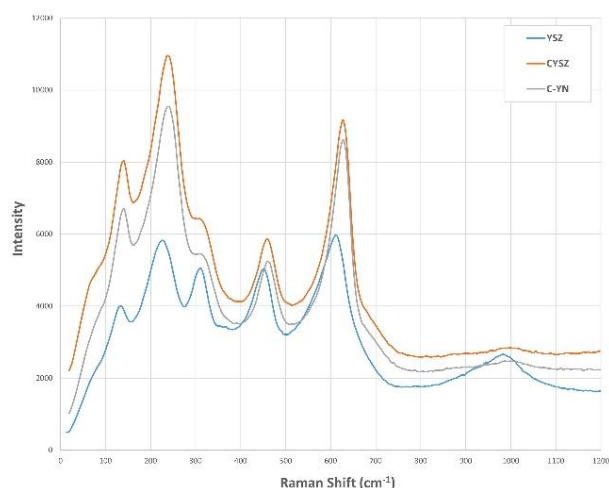


Figure 15. Raman spectroscopy results

4. CONCLUSION

Ceramic nozzles, in many cases, do not bear mechanical loads and are only responsible for controlling the flow. They do not need a metallic substrate and therefore, they can be used separately. In this study, YSZ conical nozzle is considered as the base sample for which three alternatives are designed. CYSZ is cheaper than its counterparts and is characterized by some properties such as better shock resistance. Nanostructured YSZ exhibits improved performance due to its more uniform structure and presence of nano zones, and the double-layer composite sample provides a combination of the aforementioned properties. These four samples were created through the PSF method, and their elastic modulus and hardness were determined using nanoindentation. The results showed that the nanostructured YSZ had the lowest hardness and highest elastic modulus. On the contrary, the composite sample had the lowest elastic modulus, and the YSZ sample had the highest degree of hardness.

ACKNOWLEDGEMENT

The authors thank Mapna Turbine Blade Eng. & Mfg. co. PARTO for cooperation in experimental fields.

REFERENCES

- De la Roche, J., Alvarado-Orozco, J. M., Gomez, P. A., Cano, I. G., Dosta, S., Toro, A., "Hot corrosion behaviour of dense CYSZ/YSZ bilayer coatings deposited by atmospheric plasma spray in $\text{Na}_2\text{SO}_4 + \text{V}_2\text{O}_5$ molten salts", *Surface and Coatings Technology*, Vol. 432, (2022), 128066. <https://doi.org/10.1016/j.surfcoat.2021.128066>
- Bhandari, S., Chakravarthy, Y., Misra, V. C., Tiwari, N., Lenka, R. K., Patro, P. K., Kaity, S., Satpati, S. K., Mahata, T., Ghorui, S., "Investigating Atmospheric Pressure Plasma Spray Coating of YPO_4 and its Performance as a Corrosion Barrier Protective Layer Against Molten Uranium", *Journal of Thermal Spray Technology*, Vol. 31, No. 5, (2022), 1568-1580. <https://doi.org/10.1007/s11666-022-01367-3>
- Sivaramapandian, J., Ananth, M. P., Selvabharathi, R., "Influence of plasma spray WCCrCNi coating and shot peening on surface properties and corrosion behaviour of AZ31 Mg alloy", *Journal of Materials Research and Technology*, Vol. 19, (2022), 3189-3200. <https://doi.org/10.1016/j.jmrt.2022.05.183>
- Fang, J. C., Xu, W. J., "Plasma spray forming", *Journal of Materials Processing Technology*, Vol. 129, No. 1-3, (2002), 288-293. [https://doi.org/10.1016/S0924-0136\(02\)00667-2](https://doi.org/10.1016/S0924-0136(02)00667-2)
- Li, X., Bhushan, B., "A review of nanoindentation continuous stiffness measurement technique and its applications", *Materials Characterization*, Vol. 48, No. 1, (2002), 11-36. [https://doi.org/10.1016/S1044-5803\(02\)00192-4](https://doi.org/10.1016/S1044-5803(02)00192-4)
- Wang, W., Yao, P., Wang, J., Huang, C., Zhu, H., Zou, B., Liu, H., Yan, J., "Crack-free ductile mode grinding of fused silica under controllable dry grinding conditions", *International Journal of Machine Tools and Manufacture*, Vol. 109, (2016), 126-136. <https://doi.org/10.1016/j.ijmactools.2016.07.007>
- Zhang, Z., Yao, P., Wang, J., Huang, C., Cai, R., Zhu, H., "Analytical modelling of surface roughness in precision grinding of particle reinforced metal matrix composites considering nanomechanical response of material", *International Journal of Mechanical Sciences*, Vol. 157-158, (2019), 243-253. <https://doi.org/10.1016/j.ijmecs.2019.04.047>
- Li, X., Bhushan, B., "Dynamic mechanical characterization of magnetic tapes using nanoindentation techniques", *IEEE Transactions on Magnetics*, Vol. 37, No. 4, (2001), 1616-1619. <https://doi.org/10.1109/20.950917>
- Casellas, D., Caro, J., Molas, S., Prado, J. M., Valls, I., "Fracture toughness of carbides in tool steels evaluated by nanoindentation", *Acta Materialia*, Vol. 55, No. 13, (2007), 4277-4286. <https://doi.org/10.1016/j.actamat.2007.03.028>
- Nayebi, B., Parvin, N., Shahedi Asl, M., Motallebzadeh, A., Shokouhimehr, M., "Nanostructural and nanoindentation characterization of ZrB_2 ceramics toughened with in-situ synthesized ZrC ", *International Journal of Refractory Metals and Hard Materials*, Vol. 94, (2021), 105391. <https://doi.org/10.1016/j.ijrmhm.2020.105391>
- Odegard, G. M., Gates, T. S., Herring, H. M., "Characterization of viscoelastic properties of polymeric materials through nanoindentation", *Experimental Mechanics*, Vol. 45, (2005), 130-136. <https://doi.org/10.1007/BF02428185>
- Gregory, J. R., Spearing, S. M., "Nanoindentation of neat and in situ polymers in polymer-matrix composites", *Composites Science and Technology*, Vol. 65, No. 3-4, (2005), 595-607. <https://doi.org/10.1016/j.compscitech.2004.09.001>
- Daphalapurkar, N. P., Dai, C., Gan, R. Z., Lu, H., "Characterization of the linearly viscoelastic behavior of human tympanic membrane by nanoindentation", *Journal of the Mechanical Behavior of Biomedical Materials*, Vol. 2, No. 1, (2009), 82-92. <https://doi.org/10.1016/j.jmbbm.2008.05.008>
- Gaillard, Y., Anglada, M., Jiménez-Piqué, E., "Nanoindentation of yttria-doped zirconia: Effect of crystallographic structure on deformation mechanisms", *Journal of Materials Research*, Vol. 24, No. 3, (2009), 719-727. <https://doi.org/10.1557/jmr.2009.0091>
- Cuadrado, N., Seuba, J., Casellas, D., Anglada, M., Jiménez-Piqué, E., "Geometry of nanoindentation cube-corner cracks observed by FIB tomography: Implication for fracture resistance estimation", *Journal of the European Ceramic Society*, Vol. 35, No. 10, (2015), 2949-2955. <https://doi.org/10.1016/j.jeurceramsoc.2015.03.031>

16. Pathak, S., Kalidindi, S. R., "Spherical nanoindentation stress-strain curves", *Materials Science and Engineering: R: Reports*, Vol. 91, (2015), 1-36. <https://doi.org/10.1016/j.mserr.2015.02.001>
17. Fujikane, M., Setoyama, D., Nagao, S., Nowak, R., Yamanaka, S., "Nanoindentation examination of yttria-stabilized zirconia (YSZ) crystal", *Journal of Alloys and Compounds*, Vol. 431, No. 1-2, (2007), 250-255. <https://doi.org/10.1016/j.jallcom.2006.05.058>
18. Campo, M., Ureña, A., Rams, J., "Effect of silica coatings on interfacial mechanical properties in aluminium—SiC composites characterized by nanoindentation", *Scripta Materialia*, Vol. 52, No. 10, (2005), 977-982. <https://doi.org/10.1016/j.scriptamat.2005.01.036>
19. Ulm, F. J., Abousleiman, Y., "The nanogranular nature of shale", *Acta Geotechnica*, Vol. 1, (2006), 77-88. <https://doi.org/10.1007/s11440-006-0009-5>
20. Dadfar, M. R., Rahimipour, M. R., Vaezi, M., Gholamzadeh, A., "Characterization and Phase Transformation of Spherical YSZ Powders Fabricated Via air Plasma Spray Method", *Advanced Ceramics Progress*, Vol. 2, No. 4, (2016), 32-38. <https://doi.org/10.30501/acp.2016.70034>
21. Lu, H., Huang, G., Wang, B., Mamedov, A., Gupta, S., "Characterization of the linear viscoelastic behavior of single-wall carbon nanotube/polyelectrolyte multilayer nanocomposite film using nanoindentation", *Thin Solid Films*, Vol. 500, No. 1-2, (2006), 197-202. <https://doi.org/10.1016/j.tsf.2005.11.051>
22. Saraev, D., Miller, R. E., "Atomic-scale simulations of nanoindentation-induced plasticity in copper crystals with nanometer-sized nickel coatings", *Acta Materialia*, Vol. 54, No. 1, (2006), 33-45. <https://doi.org/10.1016/j.actamat.2005.08.030>
23. Huang, G., Daphalapurkar, N. P., Gan, R. Z., Lu, H., "A method for measuring linearly viscoelastic properties of human tympanic membrane using nanoindentation", *Journal of Biomechanical Engineering*, Vol. 130, No. 1, (2008), 014501. <https://doi.org/10.1115/1.2838034>
24. Guicciardi, S., Melandri, C., Silvestroni, L., Sciti, D., "Indentation grid analysis of nanoindentation bulk and in situ properties of ceramic phases", *Journal of Materials Science*, Vol. 43, (2008), 4348-4352. <https://doi.org/10.1007/s10853-008-2657-3>
25. Botero, C. A., Jiménez-Piqué, E., Baudín, C., Salán, N., Llanes, L., "Nanoindentation of Al₂O₃/Al₂TiO₅ composites: Small-scale mechanical properties of Al₂TiO₅ as reinforcement phase", *Journal of the European Ceramic Society*, Vol. 32, No. 14, (2012), 3723-3731. <https://doi.org/10.1016/j.jeurceramsoc.2012.05.034>
26. Silva, A. P., Booth, F., Garrido, L., Aglietti, E., Pena, P., Baudín, C., "Young's modulus and hardness of multiphase CaZrO₃-MgO ceramics by micro and nanoindentation", *Journal of the European Ceramic Society*, Vol. 38, No. 4, (2018), 2194-2201. <https://doi.org/10.1016/j.jeurceramsoc.2017.11.007>
27. Bor, B., Giuntini, D., Domènech, B., Swain, M. V., Schneider, G. A., "Nanoindentation-based study of the mechanical behavior of bulk supercrystalline ceramic-organic nanocomposites", *Journal of the European Ceramic Society*, Vol. 39, No. 10, (2019), 3247-3256. <https://doi.org/10.1016/j.jeurceramsoc.2019.03.053>
28. Li, W., Liu, W., Qi, F., Chen, Y., Xing, Z., "Determination of micro-mechanical properties of additive manufactured alumina ceramics by nanoindentation and scratching", *Ceramics International*, Vol. 45, No. 8, (2019), 10612-10618. <https://doi.org/10.1016/j.ceramint.2019.02.128>
29. Szymanski, W., Lipa, S., Fortuniak, W., Chojnowski, J., Pospiech, P., Mizerska, U., Slomkowski, S., Nyczyk-Malinowska, A., Hasik, M., "Silicon oxycarbide (SiOC) ceramic microspheres—Structure and mechanical properties by nanoindentation studies", *Ceramics International*, Vol. 45, No. 9, (2019), 11946-11954. <https://doi.org/10.1016/j.ceramint.2019.03.085>
30. Zhang, Z., Yao, P., Wang, J., Huang, C., Zhu, H., Liu, H., Zou, B., "Nanomechanical characterization of RB-SiC ceramics based on nanoindentation and modelling of the ground surface roughness", *Ceramics International*, Vol. 46, No. 5, (2020), 6243-6253. <https://doi.org/10.1016/j.ceramint.2019.11.094>
31. Nayeypashae, N., Etemadi, E., Mohammad Sadeghi, B., Seyedein, S. H., "Experimental and Numerical Study of the Thermo-Mechanical Behavior of Plasma-Sprayed Gadolinium and Yttria Zirconate-Based Thermal Barrier Coatings", *Advanced Ceramics Progress*, Vol. 7, No. 4, (2021), 36-51. <https://doi.org/10.30501/acp.2022.322563.1078>
32. Zerafati, F., H. Majidian, Nikzad, L., "Dispersion Properties of Nano YSZ Particles in Aqueous Suspensions", *Advanced Ceramics Progress*, Vol. 5, No. 3, (2019), 15-22. <https://doi.org/10.30501/acp.2019.95763>
33. Bahamirian, M., "A Comparative Study on the Phase Stability of ZrO₂-8wt. % Y₂O₃: Nano- and Micro-Particles", *Advanced Ceramics Progress*, Vol. 8, No. 2, (2022), 53-60. <https://doi.org/10.30501/acp.2022.352174.1097>
34. Bahamirian, M., Hadavi, S. M. M., Farvizi, M., Keyvani, A., Rahimipour, M. R., "Thermal Durability of YSZ/Nanostructured Gd₂Zr₂O₇ TBC Undergoing Thermal Cycling", *Oxidation of Metals*, Vol. 92, (2019), 401-421. <https://doi.org/10.1007/s11085-019-09937-7>
35. Leitner, A., Maier-Kiener, V., Kiener, D., "Extraction of flow behavior and Hall-Petch parameters using a nanoindentation multiple sharp tip approach", *Advanced Engineering Materials*, Vol. 19, No. 4, (2017), 1600669. <https://doi.org/10.1002/adem.201600669>
36. Oliver, W. C., Pharr, G. M., "Measurement of hardness and elastic modulus by instrumented indentation: Advances in understanding and refinements to methodology", *Journal of Materials Research*, Vol. 19, No. 1, (2004), 3-20. <https://doi.org/10.1557/jmr.2004.19.1.3>
37. Goudarzi, Z. M., Valefi, Z., Zamani, P., Taghi-Ramezani, S., "Comparative investigation of the effect of composition and porosity gradient on thermo-mechanical properties of functionally graded thick thermal barrier coatings deposited by atmospheric plasma spraying", *Ceramics International*, Vol. 48, No. 19, (2022), 28800-28814. <https://doi.org/10.1016/j.ceramint.2021.12.307>
38. Ashofteh, A., Mashhadi, M. M., Amadeh, A., Seifollahpour, S., "Effect of layer thickness on thermal shock behavior in double-layer micro- and nano-structured ceramic top coat APS TBCs", *Ceramics International*, Vol. 43, No. 16, (2017), 13547-13559. <https://doi.org/10.1016/j.ceramint.2017.07.061>
39. Ashofteh, A., Mashhadi, M. M., Amadeh, A., "Thermal shock behavior of multilayer and functionally graded micro- and nano-structured topcoat APS TBCs", *Ceramics International*, Vol. 44, No. 2, (2018), 1951-1963. <https://doi.org/10.1016/j.ceramint.2017.10.138>
40. Łatka, L., Cattini, A., Chicot, D., Pawłowski, L., Kozerski, S., Petit, F., Denoirjean, A., "Mechanical properties of yttria-and ceria-stabilized zirconia coatings obtained by suspension plasma spraying", *Journal of Thermal Spray Technology*, Vol. 22, (2013), 125-130. <https://doi.org/10.1007/s11666-012-9874-7>
41. Adams, J. W., Ruh, R., Mazdiyasi, K. S., "Young's modulus, flexural strength, and fracture of yttria-stabilized zirconia versus temperature", *Journal of the American Ceramic Society*, Vol. 80, No. 4, (1997), 903-908. <https://doi.org/10.1111/j.1151-2916.1997.tb02920.x>
42. Okazaki, M., "Effect of microstructure on elastic modulus of YSZ thermal barrier coatings", *Journal of the Society of Materials Science, Japan*, Vol. 57, No. 11, (2008), 1121-1131. <https://doi.org/10.2472/jms.57.1121>
43. Jin, L., Yu, Q., Rauf, A., Zhou, C., "Elastic, electronic and thermal properties of YSZ from first principles", *Solid State Sciences*, Vol. 14, No. 1, (2012), 106-110. <https://doi.org/10.1016/j.solidstatesciences.2011.11.003>

44. Shimonosono, T., Ueno, T., Hirata, Y., "Mechanical and thermal properties of porous yttria-stabilized zirconia", *Journal of Asian Ceramic Societies*, Vol. 7, No. 1, (2019), 20-30. <https://doi.org/10.1080/21870764.2018.1547248>
45. Gadag, S., Subbarayan, G., Barker, W., "Thermo-elastic properties of dense YSZ and porous Ni-ZrO₂ monolithic and isotropic materials", *Journal of Materials Science*, Vol. 41, (2006), 1221-1232. <https://doi.org/10.1007/s10853-005-3660-6>